Journal of Alloys and Compounds 887 (2021) 161437

Contents lists available at ScienceDirect

Journal of Alloys and Compounds

journal homepage: www.elsevier.com/locate/jalcom

Devitrification of thin film Cu–Zr metallic glass via ultrashort pulsed laser annealing

J. Antonowicz[a,*], P. Zalden[b], K. Sokolowski-Tinten[c], K. Georgarakis[d], R. Minikayev[e], A. Pietnoczka[a], F. Bertram[f], M. Chaika[e], M. Chojnacki[e], P. Dłużewski[e], K. Fronc[e], A.L. Greer[g], C. Jastrzębski[a], D. Klinger[e], Ch. Lemke[h], O.M. Magnussen[h], B. Murphy[h], K. Perumal[f], U. Ruett[f], K.J. Warias[h], R. Sobierajski[e]

[a] Faculty of Physics, Warsaw University of Technology, Poland
[b] European XFEL, Germany
[c] Faculty of Physics and Center for Nanointegration Duisburg-Essen (CENIDE), University of Duisburg, Essen, Germany
[d] Cranfield University, United Kingdom
[e] Institute of Physics Polish Academy of Sciences, Poland
[f] DESY, Germany
[g] University of Cambridge, United Kingdom
[h] Christian-Albrechts-Universitaet Kiel, Germany

ARTICLE INFO

Article history:
Received 5 March 2021
Received in revised form 15 July 2021
Accepted 1 August 2021
Available online 3 August 2021

Keywords:
Metallic glasses
X-ray diffraction
Crystallization
Oxidation
Laser treatment

ABSTRACT

In this work we report on an ultrashort pulsed laser annealing-driven devitrification of thin film $Cu_{67}Zr_{33}$ metallic glass characterized by micro-beam X-ray diffraction and electron microscopy techniques. The essential feature of ultrashort pulsed laser annealing is ultrafast heating (10^{14} K/s) by femtosecond optical excitation followed by extremely rapid cooling (10^{10-12} K/s) due to heat dissipation into the film substrate. During repetitive optical excitation, we take X-ray diffraction snapshots of the intermediate, frozen-in stages of the glass-crystal transformation to study its kinetics. A quantitative analysis of the diffraction patterns supported by electron microscopy result shows that the glass-crystal transformation proceeds by a rapid formation of an energetically favourable layer of crystalline ZrO_2 on the free surface of the glassy film accompanied by nucleation and growth of fcc-Cu in the residual amorphous matrix. We demonstrate that at low effective annealing temperatures the devitrification kinetics of both products is correlated, while at high temperatures they decouple and ZrO_2 forms an order of magnitude faster than Cu.

1. Introduction

Metallic glasses (MGs) [1] are solids which lack long-range order in their atomic arrangement characteristic for crystalline metals. The amorphous and homogeneous nature of MGs is responsible for their numerous attractive mechanical properties, such as high yield strength and hardness, exceptional elasticity as well as an excellent wear and corrosion resistance. MGs are typically obtained by quenching a liquid alloy at a rate fast enough to bypass nucleation and growth of the competing crystalline phases and freeze the disordered atomic arrangement at the glass transition temperature. The cooling rate necessary to avoid crystallization and to form a glass (critical cooling rate) in metallic systems is usually high. However, by carefully tuning the composition of the multicomponent systems, the glass forming ability of metallic alloys can be significantly enhanced. The critical cooling rate for bulk metallic glass-formers [2] can be as low as 10^{-1}K/s. On the other hand, single-element MGs [3] require ultra-fast quenching at 10^{14} K/s to be amorphized on cooling [4].

An alternative route to obtain a metallic glass is physical vapor deposition (PVD), which can be used to produce thin amorphous films. In a PVD process such as magnetron sputtering, the effective cooling rate is typically in the order 10^{12} K/s, which makes deposition a powerful tool to obtain a variety of glassy materials [5]. Due to size effects, thin film MGs (TFMGs) are often superior to their bulk counterparts in terms of mechanical properties which makes them attractive materials for applications such as mechanically resilient coatings, biomaterials, flexible electronics or high sensitivity

* Correspondence to: Faculty of Physics, Warsaw University of Technology, ul. Koszykowa 75, 00-662 Warsaw, Poland.
E-mail address: jerzy.antonowicz@pw.edu.pl (J. Antonowicz).

https://doi.org/10.1016/j.jallcom.2021.161437
0925-8388/

microelectromechanical system (MEMS) (see [6] and references therein). One of the main factors limiting applications of glassy metals is their thermodynamically metastable state, which poses the risk of transformation to a low-energy, crystalline state at elevated temperature. Furthermore, during normal operation a functional material is usually exposed to air and thus might be prone to surface oxidation. Oxidation can be particularly important for TFMGs since the surface fraction is significantly larger than in the case of a bulk material [7]. Therefore, avoiding crystallization and oxidation of TFMGs under atmosphere and at elevated temperature is crucial for their practical implementation. Besides TFMGs, surface oxidation is also important in bulk metallic glasses used in nanodevices since thin oxide layer strongly affects their mechanical and tribological properties [8].

Alloys of zirconium and transition metals are one of the most extensively studied family of MGs and have found numerous commercial applications [9]. In particular, binary Cu-Zr MGs have been widely investigated over the past decades [10–16]. Those alloys tend to form a glass upon quenching in a wide composition range [12,15,16] and can be obtained in the form of thin films by various deposition techniques [17–19]. Cu-Zr MGs are known to suffer from rapid oxidation which proceeds by formation of a crystalline ZrO_2 on the free surface and Cu-enrichment of the sub-oxide layer [20–23]. Small addition of Be were found to stabilize an amorphous Zr oxide and inhibit oxidation of the Cu-Zr MGs [24,25]. Since the diffusivity deduced from oxidation kinetics matches that of oxygen in ZrO_2 [26], it is believed that the transformation is controlled by diffusion of oxygen towards the ZrO_2/glass interface [20]. The oxidation of Cu-Zr MGs takes place even during storage at room temperature and manifests in form of a well-known change of color of melt-spun Cu-Zr ribbons from silver to a copper-like red [27]. At elevated temperatures, the diffusivity increases and thus the oxidation process becomes significantly more rapid.

The thermal stability of MGs is usually studied experimentally by following the crystallization during annealing of the glass at temperatures of a few or a few tens of degrees above the glass transition temperature. In this temperature regime the transformation kinetics can be resolved only when the timescale of the measurement (typically seconds or minutes) matches that of the transformation kinetics [28,29]. Due to this limitation, fast, high-temperature devitrification kinetics of MG's [30,31] is extremely difficult to assess experimentally by conventional characterization techniques.

This obstacle for accessing the high-temperature glass-crystal transformation kinetics can be overcome by an approach based on ultrashort pulsed laser annealing (UPLA) which is well-suited for thin films. Optical reflectance has been used by Zalden et al. [32] to probe the frozen-in, intermediate stages of transformation to resolve ultra-fast crystal growth rates of up to 100 m/s in chalcogenide phase-change materials. The essential feature of UPLA is an ultra-fast heating (10^{14} K/s) by femtosecond optical excitation followed by extremely rapid cooling (10^{10-12} K/s) due to heat dissipation into the film substrate. This specific sample temperature profile leaves only an extremely short time window for transformation which can, due to the exponential temperature-dependence, occur effectively only at elevated temperature. The actual width of the temperature-time profile depends on the details of the film and substrate material and thicknesses but is typically of the order of nano- to microseconds.

In our current work we employ a similar UPLA approach using X-rays and electrons to probe the atomic structure of the $Cu_{67}Zr_{33}$ metallic glass. Pulsed pico- and nanosecond laser annealing has been known for many decades, and was previously used to quench metallic alloys into a glassy state [33–35] and to study phase transformations in thin film amorphous alloys [35–38]. Those studies indicate that, due to the high cooling rates, pulsed laser annealing may lead to formation of metastable amorphous or crystalline phases which cannot be formed by conventional liquid quenching. While the concept of exploiting short laser pulses for fast heating and quenching of thin metallic films is not new, there are important advantages of the current approach. Firstly, the thickness of the samples for the current study has been chosen to ensure a uniform heating of the MG film upon absorption of the laser pulse. Secondly, the conditions of the glass-crystal transformation (the effective annealing temperature and time) were systematically controlled by tuning the fluence and the number of irradiated laser pulses. This allows quasi time-resolved studies and provides a unique opportunity to study the frozen-in stages of transformations occurring on a nanosecond time scale. Finally, X-ray scattering techniques at a state-of-the-art synchrotron allow to directly monitor in situ the structural changes of the thin film samples caused by repetitive femtosecond laser irradiation.

The aim of the current work is to probe the kinetics of rapid devitrification, i.e. a process involving both oxidation and crystallization, of $Cu_{67}Zr_{33}$ TFMG in a wide range of the effective annealing temperatures and time scales, spreading over five orders of magnitude from nanoseconds up to hundreds of microseconds. By taking advantage of the opportunities offered by UPLA and microbeam X-ray diffraction we could independently follow rapid formation kinetics of different crystalline phases and propose a consistent model of thin-film $Cu_{67}Zr_{33}$ MG transformation at high temperatures and ultrafast heating rates.

2. Experimental

Metallic glass films were prepared by means of planar magnetron direct current sputtering from a $Cu_{67}Zr_{33}$ (composition in at%) target of 99.5% purity. The sputtering was carried out at room temperature. The base pressure in the sputtering chamber was approximately 8×10^{-8} mbar. During deposition, pure (99.999%) Ar gas was used at the working pressure of ~4×10^{-3} mbar. The deposition rate of $Cu_{67}Zr_{33}$ amorphous layer was ~0.4 Å/s. Optical-grade polished (0.2 nm roughness) monocrystalline silicon wafers were used as a substrate. The 500 µm thick wafers were (100)-oriented. The orientation of the Si substrate was chosen to avoid strong Bragg reflections in the X-ray diffraction pattern. Since thermal conductivity of Si crystal is at least two orders of magnitude higher than that of a typical oxide glass (more suitable for X-ray diffraction due to its amorphous structure) the monocrystalline Si substrate maximized the cooling rate of the optically-excited metallic layer. The metallic glass was sandwiched between silicon nitride layers reactively sputtered from a Si target in the presence of $Ar+N_2$ gases mixture (purity 99.999%). The bottom (buffer) layer protected the single crystal Si substrate from melting under laser irradiation, since silicon nitride has a higher melting temperature than silicon. The top (capping) layer acted as a protection of the MG against oxidation during sample storage. The effectiveness of the protection was confirmed experimentally by X-ray photoelectron spectroscopy (XPS) as well as by secondary-ion mass spectrometry (SIMS). SIMS measurements carried out shortly after deposition showed that the oxygen signal was lower than that of Zr and Cu by a factor of approximately 1000. The presence of oxygen in the metallic layer has been also excluded for silicon nitride-capped samples after the synchrotron experiment, several months after deposition. According to XPS, the atomic composition of the metallic layer in those samples was the same as that of the sputtering target. In particular, no oxygen was detected above the XPS detection limit which was better than 1 at%. The as-grown samples were characterized by means of X-ray reflectometry (XRR) and X-ray diffraction (XRD) using a laboratory radiation source. Layer thicknesses of 43.6, 31.9 and 2.3 nm were determined by XRR for silicon nitride buffer, MG and silicon nitride capping, respectively, with densities of 3.0, 7.65 and 2.7 g/cm^3 (± 1.5% for MG and ± 3.5% for silicon nitride layers), respectively. The density of the metallic layer matches well with the values

reported in the literature for Cu-Zr MGs of very similar composition [16,39]. The estimated roughness of each layer was approximately 0.5 nm. As evidenced by XRD, the as-grown layers were amorphous. Furthermore, the samples were characterized by means of ellipsometry providing information on their effective index of refraction (n = 3.16 + 3.82i) (measured for the whole coating structure) at the wavelength of 1030 nm and incidence angle of 66° selected for the UPLA.

The UPLA experiment was performed at beamline P08 of the PETRA III synchrotron (DESY, Hamburg) [40]. For optical excitation, a femtosecond laser, operating at a wavelength of 1030 nm emitting 250 fs long pulses at repetition rates up to 50 Hz, was used. The optical beam was focused at the sample position down to a spot size of ~350 μm diameter corresponding to ~2.5 × 10^5 μm^2 effective area of the beam footprint at the sample with an angle of incidence of 66 ± 0.5° (with respect to the surface normal). The maximum incident radiation fluence at the interaction point was ~60 mJ/cm^2 for 140 μJ pulse energy. To increase the absorption of the radiation, the incident laser beam was p-polarized with respect to the reflection plane. The X-ray photon energy was tuned to 25 keV. The diffracted beam was measured with a 2D large area Perkin Elmer flat-panel detector (size 41 ×41 cm^2) at a distance of 390 mm from the sample. This gives access to a momentum transfer of up to 5 Å^{-1} ($q = 4\pi\sin\Theta/\lambda$ with Θ is half of the scattering angle and λ is the X-ray wavelength), which is sufficient to capture the first and second structure factor peaks of the MG. The XRD patterns were collected at a grazing incidence angle of 1° (89° with respect to the surface normal) to increase the scattering signal from metallic film over the background caused by thermal diffuse scattering from the crystalline substrate. The focused X-ray beam had a size of ~ 2 × 20 μm^2 (vertical × horizontal direction, respectively). Its footprint on the sample at the grazing incidence (~115 ×20 μm^2) was about 5 times smaller than the laser spot size and thus the X-ray beam probed a uniformly laser-affected region of the film. The experiment was performed at the P08 Kohzu diffractometer under ambient conditions in air. The single-image exposure time was set to 0.1 s and 10 consecutive images were averaged to increase the signal-to-noise ratio resulting in an effective acquisition time for a single XRD pattern of 1 s. The laser repetition rate was adjusted to the required resolution in the pulse number domain, with 50 Hz being chosen for long effective annealing times and 1 Hz (or lower) for capturing the structural changes from pulse-to-pulse.

The irradiated spots were further investigated post-mortem by means of laboratory techniques in a similar way to the one described in reference [41]. The surface morphology was studied by means of scanning electron microscopy (SEM). Following Liu's approach [42], the spatial fluence distribution of the laser pump beam (including the effective beam area necessary to calculate the fluence) was determined from an analysis of the modified surface area as a function of laser pulse energy.

Selected spots on the sample were studied by means of transmission electron microscopy (TEM) using a FEI Titan CUBED 80-300 microscope operating at 300 kV acceleration voltage equipped with energy dispersive X-ray analysis (EDX) analyzer. Subsequent to laser irradiation all samples were capped with a thin protective layer of Pt and ~50 nm thick cross-sections were cut by a focused ion beam in preparation for the TEM measurements.

3. Results

3.1. Ultra-short pulsed laser annealing

The general concept of UPLA is shown schematically in Fig. 1 where the process is divided into consecutive steps (A–D). In the first step (A) the thin MG film deposited on a thick, thermally conductive substrate is irradiated with a femtosecond optical laser pulse. The pulse energy is absorbed in the film and leads to its local heating, typically within a few ps by relaxation of the photo-excited carriers through electron-phonon coupling [43] (B). Due to the transient increase of the atomic mobility at elevated temperatures, the film can undergo (partial) structural transformations before the excited volume cools down by rapid dissipation of heat into the substrate (C). Therefore, the structure of the intermediate, partially transformed state is frozen-in at room temperature and can be probed at any time scale by X-rays or electrons (D). After capturing the intermediate state of the sample, the A-B-C-D sequence can be repeated any number of times, giving access to the subsequent stages of devitrification. In this way, the material can by annealed in a stepwise mode with the maximum annealing temperature determined by the laser fluence F and the effective annealing time proportional to the number of laser pulses N. As shown below by the results of numerical modelling, a single pulse corresponds to an effective annealing time of the order of a few nanoseconds. Thus, the UPLA technique allows transformations to be probed on very short time scales, which are not accessible via conventional experimental methods.

For a given sample design and a given laser pulse fluence, the time-dependent temperature distribution can be derived numerically under certain assumptions discussed in the following paragraph. The first assumption concerns the distribution of the absorbed laser pulse energy in the irradiated film. The in-depth profile of the absorbed energy density can be calculated from the optical constants of the material and the incident laser pulse fluence [44]. Initially, within the metallic layer, it follows approximately the exponential decrease with characteristic absorption depth of 17 nm (with minor deviations related to the fact that the sample has a layered structure and is not a bulk material). Before the energy absorbed by the electrons is transferred to the atoms (with the process occurring on a time scale of a few ps), the heat disperses over the thermal diffusion length of approximately 20–30 nm (calculation are based on the thermodynamic data provided in Ref. [43]) leading to a quasi-uniform temperature profile over the whole depth of the metallic layer. Furthermore, the energy diffusion within the excited electron gas is much faster than the typical heat transfer at a metal-SiN interface [45], which occurs (according to our simulations described below) on a time scale of hundreds of ps and longer. Thus, we assume that the absorbed energy and the resulting initial temperature for heat transport simulations are uniform throughout the MG layer.

Fig. 2a presents the results of numerical simulations of the film temperature evolution for selected laser fluence values corresponding to the upper and lower boundaries of fluence used in the current study. The simulated maximal temperature reached by the film is around 570 K for F = 9 mJ/cm^2 and around 1550 K for F = 60 mJ/cm^2. Comparing these values to characteristic temperatures of $Cu_{67}Zr_{33}$ alloy shows that the lowest F pulse heats the film to about 175 K below the glass transition temperature [46] while the highest F pulse increases the temperature about 300 K above the liquidus. Furthermore, the maximal temperature rise (measured from 300 K) is approximately proportional to F. The corresponding temperature-dependent cooling rates (Fig. 2b) mostly span values in the range $10^{10} - 10^{12}$ K/s. They are approximately given by $\sigma \times \Delta T / (d \times C_p)$, with ΔT being the temperature difference across the metal-silicon nitride interface, σ the thermal boundary conductance at the same interface, C_p the heat capacity of the MG, and d the MG film thickness. The temperature dependence of C_p was taken from the fits to the experimental data reported in [46] for Cu–Zr amorphous and supercooled liquid alloys. Namely, we assumed a linear temperature dependence of heat capacity between the room and the glass transition temperature (T_g), and approximated the excess C_p of the supercooled liquid (above T_g) by the polynomial equation suggested by Kubaschewski [47]. The value of thermal boundary conductance was

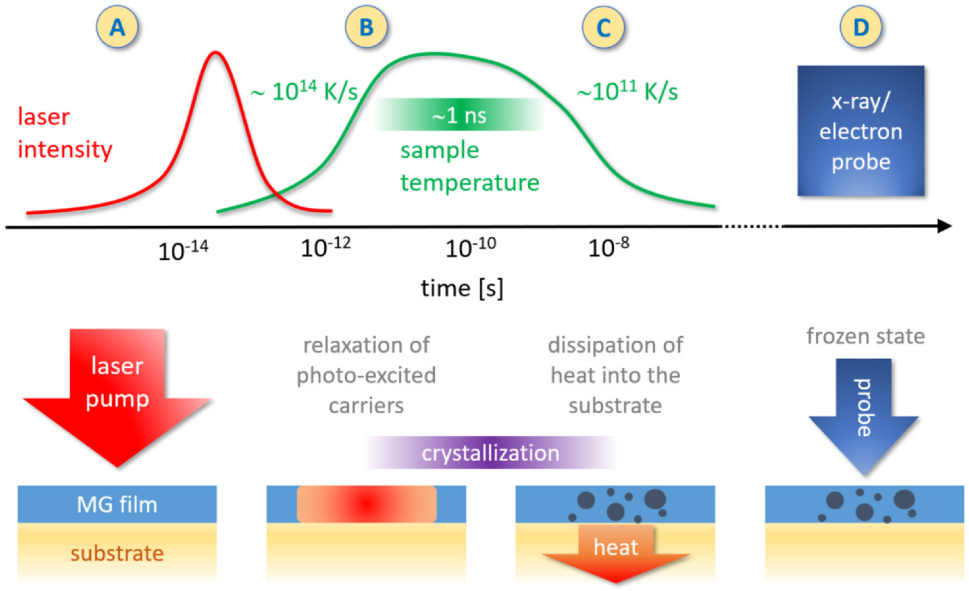

Fig. 1. Schematic concept of an ultrashort pulsed laser annealing approach. The cycle is repeated *N* times to compare the initial state (separate probe event, not indicated in the figure) with that probed after the *N* cycles.

taken as 125 MW/m^2/K, corresponding to σ measured for Au/SiN interface [45]. To visualize the effect of variation of σ on the temperature evolution, temperature-time and cooling rate- temperature functions calculated for 5 times lower (σ = 25 MW/m^2/K) and 5 times higher (625 MW/m^2/K) boundary conductance have been plotted at F = 60 mJ/cm^2 in Fig. 2a and b. As expected, the cooling rate scales with σ, and thus enhanced thermal conductance results in a shorter time spent by the film in the high-temperature regime. Judging from

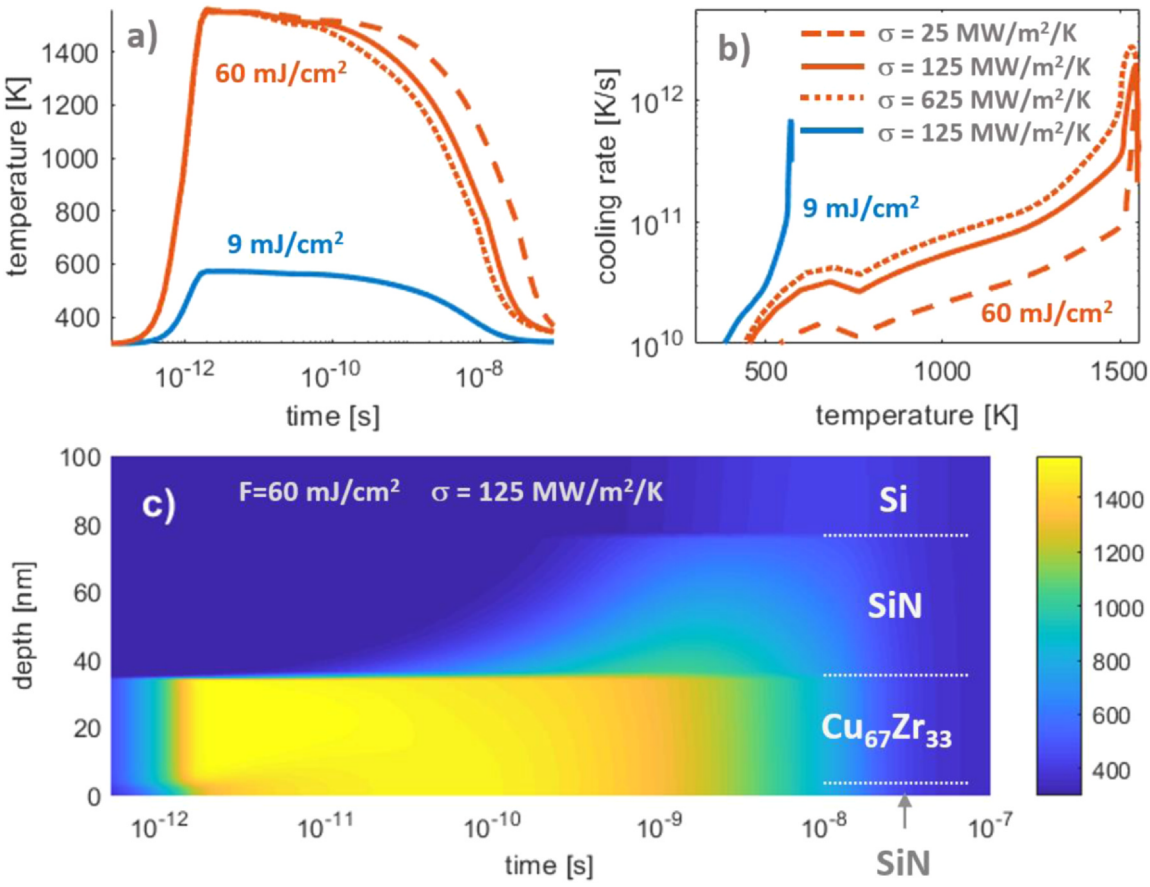

Fig. 2. Simulated temperature-time (a) and cooling rate-temperature (b) functions and time-dependent temperature distribution inside the sample at the minimum (F = 9 mJ/cm^2) and the maximum (F = 60 mJ/cm^2) laser fluence used in the experiment. Solid lines (a, b) and colour map (c) correspond to a thermal conductance at the MG-Si_3N_4 interface of σ = 125 MW/m^2/K. The dotted and dashed lines in (a, b) were calculated for F = 60 mJ/cm^2 and thermal conductance at the interface equal to σ = 625 MW/m^2/K and σ = 25 MW/m^2/K, respectively.

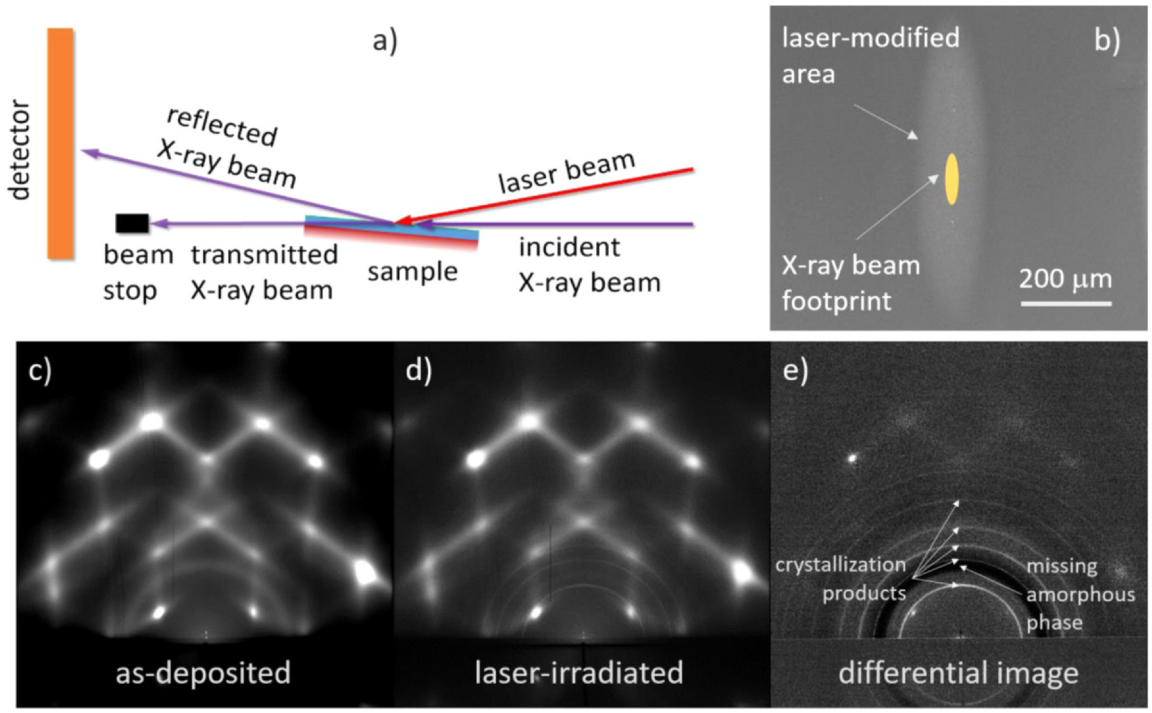

Fig. 3. Schematic layout of the grazing-incidence XRD experimental setup (a). SEM image of a laser-modified area with marked size of an X-ray beam footprint on the sample surface (b). 2D XRD patterns of the as-deposited (c) and laser-irradiated (F = 60 mJ/cm^2, N = 350) (d) MG film are dominated by thermal diffuse scattering from the Si substrate. Weak rings from the metallic layer are seen in the bottom of both images, The differential image (e) resulting from subtraction of the image (c) from (d) shows a broad dark ring corresponding to the missing amorphous phase in the irradiated sample (d) and fine bright rings originating from the crystallization products.

Fig. 2a, an increase of σ by a factor of 5 decreases the duration of the high-temperature stage by a factor of ~2. It thus follows that within a reasonable range of σ values the effective time spent by the film in the high-temperature regime is of the order of a nanosecond.

The fast temperature changes in the process described above are not compatible with common techniques to determine the actual temperature of the sample, so in this work we provide the fluence deposited by the laser and estimate the corresponding temperature jump based on the model of heat transport in the film and substrate. Furthermore, the estimation of the maximum temperature of the MG layer depends on the calculations of deposited heat and is affected by a collection of uncertainties on deposited energy density (depending on laser pulse energy, spot size determination, angle of incidence and estimation of optical properties and thermodynamic properties of materials involved - heat capacity and thermal conductance). In particular, it may lead to an overestimation of the maximum sample temperature, which in our experiment does not exceed above the liquidus for the case of F = 60 mJ/cm^2. We argue that since sample melting would be manifested by a sudden variation of the transformation kinetics as well as a change in typical surface features and none of those has been detected in our study, melting is not involved. Nevertheless, the essential characteristics of the temperature-time profile do not depend strongly on the exact values of the thermodynamic properties of the materials involved. Thus, as shown above, some approximations can be made, which allow a reasonable estimation of both the maximum sample temperature and the cooling rate.

Another challenge is possible heat accumulation upon repetitive laser irradiation. The essential assumption of the UPLA is that after optical excitation the sample cools down to room temperature before it absorbs the subsequent laser pulse. At sufficiently high laser repetition rates this assumption is not satisfied and accumulation of heat would accelerate the transformation kinetics. To eliminate these effects, we applied laser pulse repetition rates ranging from 1 to 50 Hz in the current study. By comparing the kinetics for the same number of pulses but different repetition rates for selected fluences, we verified that in this frequency range the transformation progress does not depend on the repetition rate and scales solely with the number of laser pulses. This observation agrees with numerical solutions of the heat-diffusion equation, which show that the frequency of 50 Hz is sufficiently low to completely exclude heat accumulation. It follows that the effective annealing time scales strictly with the number of applied pulses. The maximum number of pulses used in the current study was 2×10^5, which corresponds to an effective annealing time of the order of hundreds of microseconds.

Apart from accumulation of heat, one has to consider build-up of surface modifications leading to a variation of scattering properties due to increased roughness and/or modifications of the index of refraction related to chemical and concentration changes. Those changes may in turn lead to variation of the maximum temperature reached by the film upon multi-pulse irradiation. These complex effects are difficult to include in numerical simulations in a reliable way. For this reason, we use the laser fluence (which was actually controlled throughout the experiment) rather than temperature as the parameter characterizing the transformation kinetics. For consistency, we also use the number of laser pulses instead of effective annealing time to describe the transformation progress. Keeping in mind that the effective annealing temperature increases monotonically with F, and N is proportional to the effective annealing time, each of the XRD patterns and TEM images has been assigned a specific pair of variables F and N, which completely describe the conditions of the transformation.

3.2. In-situ XRD results

A schematic layout of the grazing-incidence XRD experimental setup used during the synchrotron experiment is presented in Fig. 3a

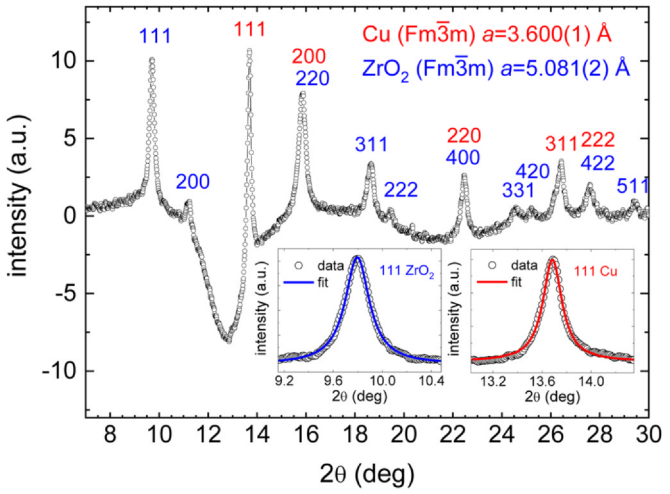

Fig. 4. Azimuthally integrated differential XRD pattern of a fully crystallized MG film (F = 60 mJ/cm^2, N = 350) at 25 keV. The Bragg peaks belonging to Cu (red) and ZrO_2 (blue) crystalline phases are indexed. The insets shows ZrO_2 (111) and Cu (111) peaks, fitted by a Lorentzian function.

and b shows SEM image of a laser-modified area with marked size of an X-ray beam.

In order to quantitatively analyze the XRD data, the 2D differential patterns were azimuthally integrated by means of the pyFAI software [48]. First, the necessary geometrical corrections, image subtraction, azimuthal integration, and normalization to the incident X-ray intensity were applied and the peak position and instrumental peak broadening were calibrated with the help of measurements of a standard reference material (LaB_6). For the image in Fig. 3e, the resulting intensity as function of the scattering angle 2Θ is shown in Fig. 4. A quantitative analysis of the pattern shows that all peaks can be attributed to Bragg reflections of two crystalline phases: (i) cubic Cu ($Fm\bar{3}m$) with a lattice constant a = 3.600(1) Å and (ii) cubic ZrO_2 ($Fm\bar{3}m$) with a lattice constant a = 5.081(2) Å. The broad, negative peak centered at about 2Θ = 13° and the depression of the curve located around 2Θ = 23° are the first- and the second-order structure factor peaks of the $Cu_{67}Zr_{33}$ glass which has transformed into crystalline phases upon annealing. We find no indication for the formation of crystalline Cu-Zr intermetallic compounds or metallic Zr. Judging from the intensity of the Cu and ZrO_2 Bragg peaks, the volume fraction of the two phases is comparable when the crystallization process is completed.

To access the kinetics of formation of the crystalline phases, we carried out Bragg peak profile analysis of the differential XRD patterns acquired for different F and N. For the peak fitting we have chosen a Lorentzian function:

$$y = y_o + \frac{2A}{\pi}\frac{w}{4(x - x_c)^2 + w^2}$$

where y_0 is the peak offset, A the area, w the full width at half maximum, and x_c the peak position. This function was found to accurately reproduce the actual Bragg peak profile (after linear baseline subtraction), as demonstrated by exemplary results of the peak fitting for the ZrO_2 (111) and Cu (111) reflections (inset of Fig. 4). We use all parameters of the Lorentzian fit, namely peak position, area and width, to characterize the transformation process. Assuming non-textured growth, the integrated scattering intensity of any particular diffraction peak (approximated by the area of the Lorentzian function) represents a relative measure of the volume fraction of the corresponding phase. From the peak width, we estimate the average grain size, using the Scherrer equation [49], taking instrumental broadening into account. Finally, examining the peak position relative to the nominal value (calculated from the known, equilibrium lattice parameters of 5.1280 Å and 3.61491 Å for ZrO_2 [50] and Cu [51], respectively) allows conclusions on the strain.

Similarly, Gaussian fits of the broad peak originating from the amorphous phase were carried out (for the non-differential XRD patterns) to extract supplementary information on the kinetics of the devitrification process. The integrated scattered intensity of the amorphous peak (approximated by the area of the Gaussian function) represents the relative measure of the volume fraction of the amorphous phase. From the position of the peak, the concentration of Cu in the alloy was derived applying the linear relation established in Ref. [16] for Cu–Zr MGs. Due to the overlap of the amorphous halo and the Bragg peaks, the reliable fits for the amorphous phase were possible only for the initial/intermediate stages of the devitrification. At further advancement of transformation, the parameters of the Gaussian peak become significantly affected by strong Bragg peaks. The lower limit for the reliable amorphous peak fitting was arbitrarily set at approximately 30% of its initial (maximum) intensity.

Results of such an analysis as a function of the number N of applied laser pulses are presented in Fig. 5 for a "low" (16 mJ/cm^2; left panel) and a "high" fluence (60 mJ/cm^2; right panel). Fig. 5a and b compare the integrated intensity of the (111) diffraction peaks of the crystalline ZrO_2 and Cu phases. For low laser fluence (Fig. 5a), the precipitation of cubic ZrO_2 and Cu from the amorphous matrix occurs at a similar rate. Devitrification under these conditions proceeds as a regular decomposition into two constituents: the Cu expelled by the crystallization of ZrO_2 gradually crystallizes, or equivalently, the excess Zr from crystallization of Cu, oxidizes at the surface. Repeating the devitrification at high fluences (Fig. 5b), however, reveals a decoupling of the crystallization kinetics of the two phases. Here, the formation of ZrO_2 is completed after a few ten pulses while the Cu-signal saturates only at $N \approx 350$. This shows that oxidation of Zr at the surface is the energetically dominant mechanism and is favorable even without the enthalpy gain due to the formation of crystalline Cu. As shown in Fig. 5a and b, the kinetics of formation of crystalline products of devitrification is correlated with the rate of decrease of the contribution of the amorphous phase. The decrease is accompanied by a systematic shift of the position of the amorphous peak (not shown) towards higher diffraction angles, from the initial value of about 12.9° to about 13.1° in the 2Θ scale. This shift can be attributed to the change of the Cu concentration in the MG from the initial 66 at% of Cu (as measured by XPS for the as-deposited sample) towards higher concentrations (up to 70 at% of Cu within the reliable amorphous peak fitting range). The observed enrichment of the amorphous phase in Cu is in agreement with the described above scenario of surface oxidation of Zr species.

The N-dependences of the average ZrO_2 and Cu grain sizes are depicted in Fig. 5c and d. At low fluence, the mean grain size remains at near constant values of about 8 nm and 15 nm for ZrO_2 and Cu, respectively. This can be rationalized by considering that since the crystallizing phase has a different stoichiometry than the surrounding material and thus the crystallization process is diffusion-limited, a local depletion will occur, limiting the final grain size. At high fluence, when ZrO_2 crystallizes first, the concentration of Cu in the remaining amorphous material increases gradually and enables the formation of larger Cu crystallites during the later stages of the devitrification. We will show later based on TEM images that this enrichment of Cu is not limited to the interface with the crystalline ZrO_2, but most likely occurs over the entire depth of the film.

Fig. 5e and f shows the evolution of crystalline lattice strain calculated from a ratio between the fitted and the nominal (equilibrium) (111) peak position. Independent of fluence, the peaks of both, ZrO_2 and Cu, are shifted to larger diffraction angles (relative peak position > 1) indicating compressive strain. The saturation levels of the relative peak position/compressive strain are similar for both fluences. However, the strain present in the oxide (~1%) is by a

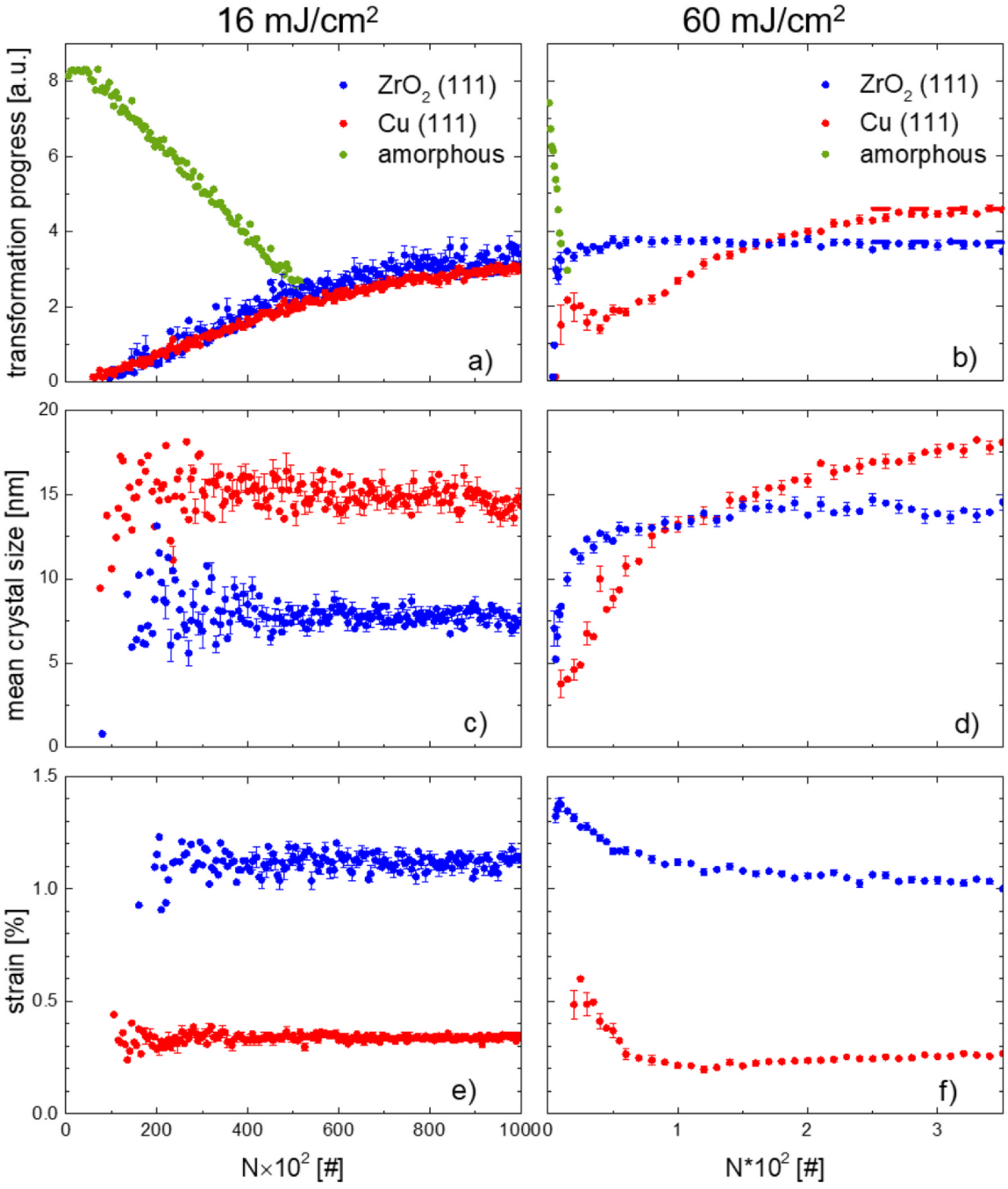

Fig. 5. Response of the ZrO_2(111) – blue, Cu (111) - red and amorphous – green peaks to number of laser pulses, up to $N = 10^5$ for low fluence (left) and up to $N = 350$ for high fluence (right). The transformation progress (a, b), mean crystal size (c, d) and the strain (e,f) derived from fits of the amorphous and (111) peaks of ZrO_2 and Cu are shown. The maximal peak intensities, corresponding to a completely crystallized sample, are marked in Fig. 5b for ZrO_2 and Cu (blue and red dashed lines, respectively). For clarity, every second error bar is plotted.

factor of about 4 higher than that in metallic copper (~0.25%). For low fluence, the strain in both crystalline phases remains almost constant during annealing, while in the case of high fluence, the strain progressively relaxes with increasing number of laser pulses. This observation indicates that in the beginning of the devitrification induced by high-fluence pulses compressive stress builds up in the crystalline lattice of ZrO_2 and (to a smaller extent) of Cu, which partially relaxes with further annealing.

To visualize the overall transformation kinetics, Fig. 6 shows the values of F as a function of N required to reach 5% (open symbols) and 33% (filled symbols) transformation progress for the ZrO_2 (blue) and Cu (red) phases. For each phase the transformation progress was determined from the integrated intensity of the corresponding (111) Bragg peaks relative to the observed maximum values (3.7 a.u. and 4.5 a.u. for ZrO_2 and Cu, respectively, as marked by the dashed lines in Fig. 5b). 5% and 33% levels were selected because the former marks the onset of the transformation, whereas the latter is the highest value that was reached during the observation time for all fluences above 10 mJ/cm^2. The number of pulses necessary to increase the crystalline fraction from 5% to 33% is also a measure of the initial rate of the glass-crystal transformation. As discussed in the previous paragraph, the formation of ZrO_2 and Cu phases exhibits similar kinetics at low fluence and a decoupling of the kinetics involving a considerable acceleration of ZrO_2 crystallization with

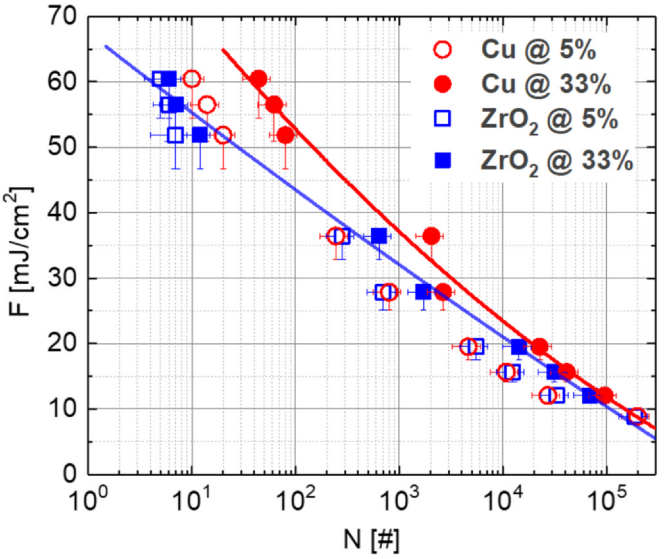

Fig. 6. *N*-dependent selected values of transformation progress (5% and 33% of the maximal observed phase content) of zirconium oxide (blue symbols) and metallic copper (red symbols) plotted for all values of laser fluence. Solid lines are a guide for the eye for 33% transformation progress.

respect to that of Cu at high fluence. As shown by the data in Fig. 6, the transition between these regimes occurs between 30 and 50 mJ/cm^2. Below 30 mJ/cm^2 precipitation of ZrO_2 and Cu from the amorphous phase occurs simultaneously with the rate of formation of Cu crystals only slightly lower than that of ZrO_2. Above 50 mJ/cm^2, ZrO_2 crystallization is clearly accelerated and its onset significantly precedes that of Cu crystallization. The trend is found up to the highest fluence used in our study (60 mJ/cm^2).

3.3. Electron microscopy analysis

The surface morphology of films studied in the synchrotron experiment was characterized ex situ by scanning electron microscopy (SEM). Due to the Gaussian fluence distribution of the pump laser on the sample, different regions of the laser-modified zone (Fig. 2b) were exposed to a different effective fluence during irradiation. This results in a spatial distribution of the characteristic surface features which develop during repetitive laser irradiation. Fig. 7 displays typical laser-induced surface modifications appearing successively with an increasing dose $D = N \times F$. As shown in Fig. 7a, the sample in the as-prepared state exhibits some sub-micrometer features visible as darker spots. The first indication for UPLA-induced surface morphology modification is the appearance of a regular, wavy pattern (Fig. 7b), corresponding to ripples at a lateral length scale of several ten nanometers, which correspond to a modulation of the surface topology with a periodicity scaling with the wavelength of the inducing light [52]. On further irradiation, damage of the film sets in. The damage is initiated by localized fracture and partial removal of the film material, resulting in the appearance of small craters (Fig. 7c). We suggest that the damage originates from surface defects in the as-prepared state. Such “weak spots” are more prone to fracture and film delamination than the non-defective regions. Further film damage and progressive material removal at higher *N* is correlated with an apparent drop of the scattered X-ray intensity. We note that data collected for considerably damaged films were excluded from the XRD analysis above and are not considered in this work. Since ripples and craters can be distinguished in the SEM image, we could determine their external contours and establish a relation between the amount of modified surface area and the irradiation dose. By comparing areas enclosed by such contours with the beam profile defined by the fluence scans [53] we were able to calculate the threshold fluences at which different morphologies are induced as a function of *N*. The *N*-dependent threshold values for surface waviness and fracture are plotted in Fig. 7d.

To get further insight into the mechanism of laser-induced devitrification, spots irradiated with various numbers of laser pulses of different fluences were structurally examined by TEM (see Fig. 8), together with EDX studies of the chemical composition. The cross-section of the as-deposited sample (Fig. 8a) consists of ~33 nm of Cu-Zr MG between ~45 nm buffer and ~3 nm capping amorphous silicon nitride layers, in good agreement with the results of the XRR measurements. The small contrast modulations visible inside the MG film were investigated by EDX and found to correspond to local variations in concentration of about ± 5 at%. For a sample irradiated with a single laser pulse of 60 mJ/cm^2 (Fig. 8b), a thin (~3 nm) layer of a new phase formed on the surface of the film, which manifests in the TEM image as a dark grey region and is composed of zirconium and oxygen atoms according to the EDX analysis. Irradiating the sample with 10 pulses of 60 mJ/cm^2 results in a thickening of the oxide layer to ~8 nm (Fig. 8c). Upon further irradiation ($N = 100$), the oxide layer grows to ~15 nm and fcc-Cu grains appear in the initially amorphous film (Fig. 8d). However, not the entire amorphous film has crystallized, as expected from the intensity of Bragg diffraction after this treatment, and the fcc-Cu grains are not dominantly formed at the ZrO_2 interface, indicating that fcc-Cu nucleates homogeneously even at high fluence conditions. A detailed analysis of the HRTEM data collected for the sample irradiated with 100 pulses of 60 mJ/cm^2 (Fig. 8e) allowed to identify two crystalline phases: Cu (Fm$\bar{3}$m) and ZrO_2 (Fm$\bar{3}$m), which is in agreement with the XRD results. A HRTEM image of an interface between the metallic film and the amorphous SiN buffer of the same specimen is shown in Fig. 8f. The sharp interface visible in Fig. 8f indicates that interdiffusion between SiN and metal was negligible both in the as-grown and the irradiated samples. It is worth mentioning that a comparison of the cross-section TEM micrographs taken for different values of *N* revealed an increase of the film thickness along with UPLA. We found that the as-deposited metallic film of ~33 nm progressively increases its thickness by approximately 2, 4 and 6 nm after irradiation with 1, 10 and 100 pulses, respectively. The increase of the overall (metallic plus oxide) film thickness is attributed to incorporation of oxygen from the atmosphere upon formation of ZrO_2.

4. Discussion

The objective of this study was an experimental investigation of the rapid devitrification of $Cu_{67}Zr_{33}$ TFMG during annealing in air. To access the fast high-temperature kinetics of the glass-crystal transformation we employed a novel method based on a step-wise annealing of the film by ultrashort laser pulses and probing the intermediate, frozen-in stages of transformation by grazing-incidence X-ray diffraction and TEM. In order to inhibit the uncontrolled oxidation of the as-deposited film we used a thin amorphous SiN protective capping which acts as an efficient barrier for oxygen diffusion during sample storage but on laser irradiation becomes immediately permeable for oxygen. Whether the effect is due to damage of the thin capping layer, caused by a laser-induced pressure/strain wave, or by other factors, is beyond the scope of this paper. Regardless of its origin, this effect allows to probe the initial stages of devitrification of an initially amorphous and non-oxidized film.

The current experimental results show that UPLA of $Cu_{67}Zr_{33}$ TFMG leads to transformation into cubic zirconium oxide and metallic fcc copper phases. No traces of other crystalline phases were detected by XRD or TEM in the irradiated films. The above phase transformation differs from that typically reported for Cu–Zr glassy

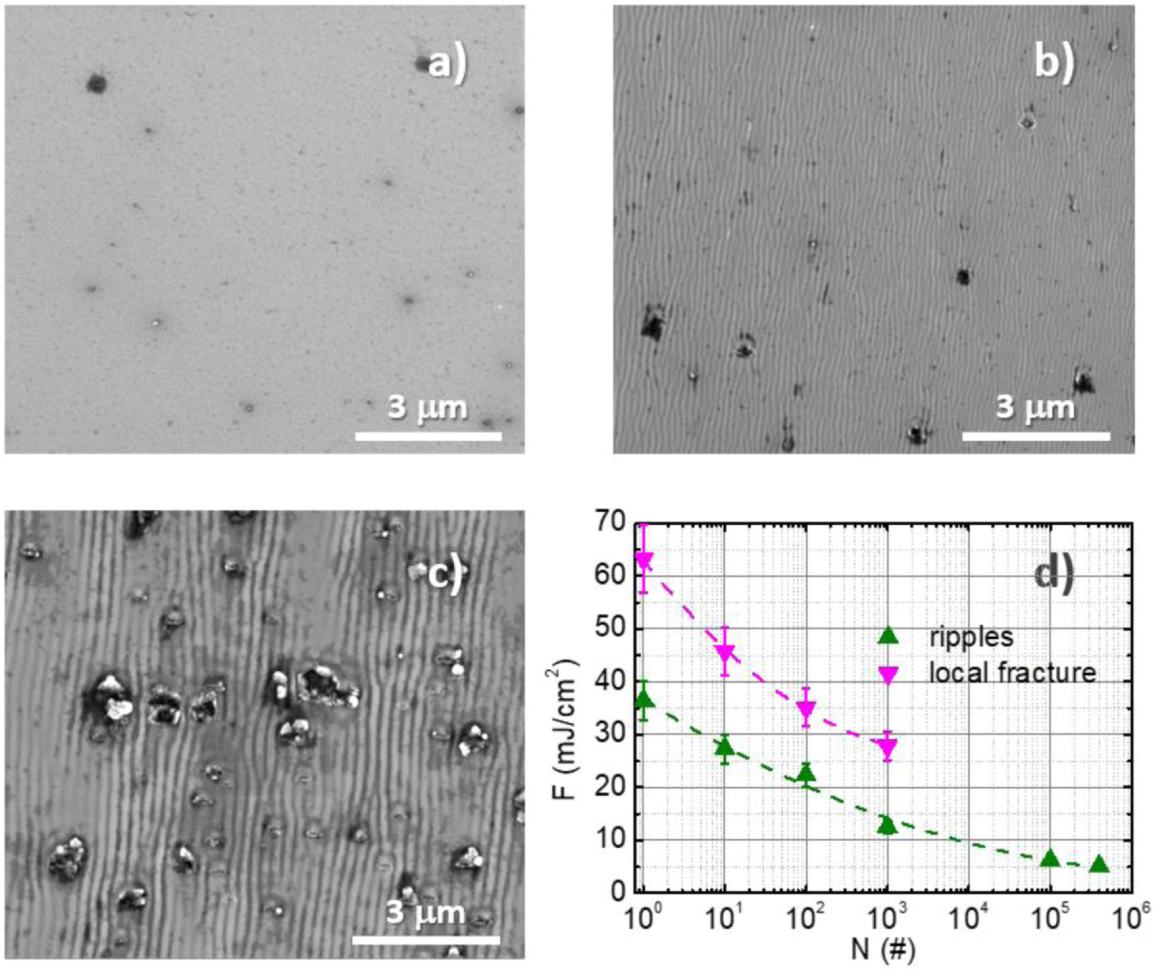

Fig. 7. SEM images showing typical surface features during UPLA. Upon laser irradiation, the as-deposited film (a) exhibits sub-micrometre ripples (b) and subsequently undergoes damage by local fracture (c). *N*-dependent fluence thresholds for ripples and local fracture are marked with symbols in (d). The dashed lines are a guide to the eye.

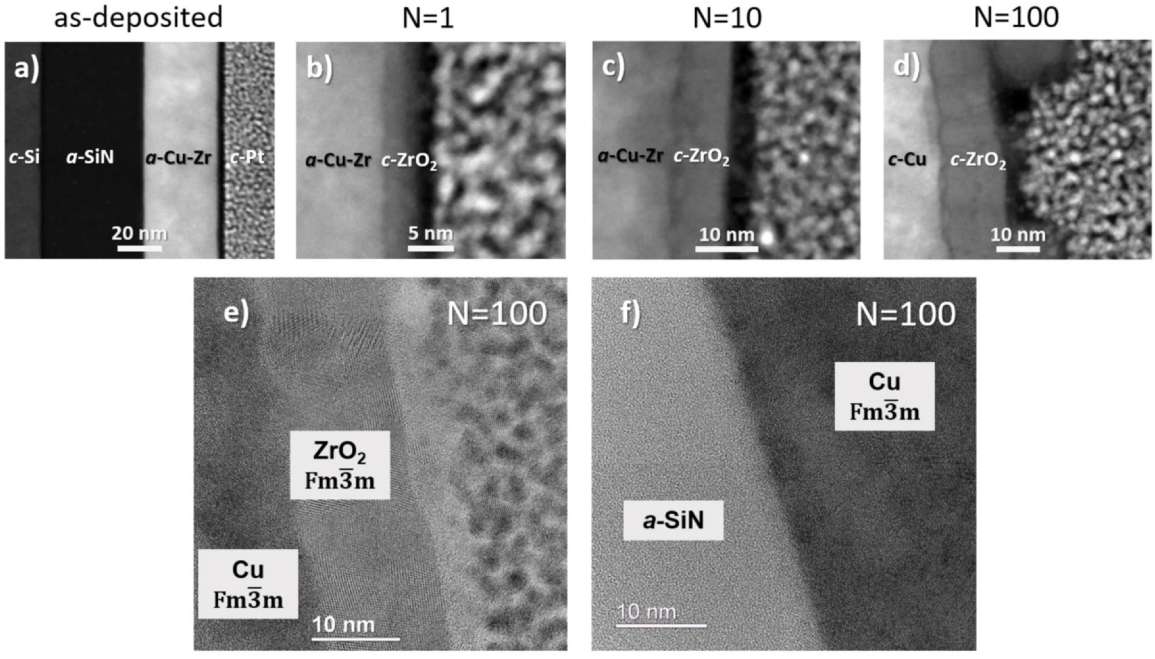

Fig. 8. Cross-section TEM micrographs of the as deposited (a) and laser-irradiated (60 mJ/cm^2) films (b–d). Prefixes *a* and *c* refer to amorphous and crystalline phases respectively as confirmed by selected-area electron diffraction. High-resolution TEM of the film irradiated with 100 pulses (60 mJ/cm^2) showing the ZrO_2 layer region (e) and an interface between the metallic film and the amorphous SiN buffer (f). In (e) and (f) denoted are phases identified by fast Fourier transform of the selected areas of the image.

ribbons, which on annealing tend to form one or more Cu–Zr intermetallic compounds present in the equilibrium Cu–Zr phase diagram [54]. We attribute it to a different transformation pathway during UPLA of $Cu_{67}Zr_{33}$ TFMG, where Zr rapidly diffuses to the surface of the film, driven by the enthalpy gain due to nucleation of ZrO_2 and resulting in an enrichment of the sub-surface region in Cu, which is expelled from the MG during Zr oxide formation. This effect, driven by high affinity of Zr for oxygen, is responsible for an in-depth compositional variation.

Some aspects of phase selection in UPLA are worth discussing in more detail. Firstly, formation of a cubic polymorph of zirconium dioxide is a rather unexpected effect since cubic ZrO_2 is thermodynamically stable only above 2370 °C. The equilibrium state of ZrO_2 at room temperature is a monoclinic phase which transforms into a tetragonal structure at 1443 K [55]. Most published works on the oxidation of Zr-based MG report the formation of monoclinic and tetragonal ZrO_2 [56,57], but in some studies their coexistence with minor amounts of cubic ZrO_2 is mentioned [20,58]. The current data show that cubic ZrO_2 is the only polymorph of zirconium oxide identified both by XRD and TEM, independently on laser fluence and number of laser pulses. Furthermore, the cubic phase remains stable at room temperature for an extended period, since it was observed by the TEM several months after the synchrotron experiment. In our interpretation, the stabilization of the high-temperature cubic ZrO_2 is due to incorporation of Cu atoms in the crystalline structure of the oxide. According to literature, the high temperature tetragonal and cubic phases of ZrO_2 can be stabilized at room temperature by adding appropriate dopants or by exploiting size effects [59,60]. In particular, the stability of Cu-doped cubic ZrO_2 nanocrystalline powders has been reported to extend down to room temperature upon Cu addition in the range of 1–25 at% [61]. The authors of ref. [61] observed a shrinkage of the unit-cell constant from 5.118 Å to 5.106 Å with increasing the Cu content and a similar trend is present in our XRD data. In our case, however, the lattice constant is even lower (5.081 Å), although the EDX analysis of the ZrO_2 layer suggests that the Cu content in the oxide region does not exceed 10 at%. This indicates that the lattice constant is affected both by the presence of Cu atoms and by a compressive stress developing during formation of the oxide and it partial relaxation, as shown in Fig. 5f.

While the extended stability of cubic ZrO_2 can be explained by Cu doping, the question remains why cubic ZrO_2 is formed in UPLA and not during conventional annealing of bulk and TF Cu–Zr MGs. In our opinion, this difference is caused by the highly non-equilibrium conditions under which UPLA occurs. In contrast to conventional annealing, which employs low heating/cooling rates, devitrification upon UPLA involves extremely rapid temperature variations and ultrafast transformation rates. According to our results, a time window of the order of a nanosecond (one laser pulse of 60 mJ/cm^2, see Fig. 2a) is sufficient for a 3 nm thick layer of an oxide to form (Fig. 8b). The above implies that the initial oxidation front proceeds at a rate reaching meters per second which is many orders of magnitude higher than the rate of oxidation observed during conventional heating of Cu–Zr MGs [2,20]. At such high interface velocities, substantial solute trapping occurs [62,63] leading to extreme supersaturations extending up to five orders of magnitude beyond the equilibrium solubility [64]. While during conventional annealing oxidation occurs on a sufficiently long time scale for Cu partitioning between the oxide and the glassy phase, the in-depth diffusion of small oxygen atoms [65] is considerably faster than that of copper during UPLA. As a result, Cu atoms become partially trapped behind the progressing crystalline oxide/amorphous metal interface and stabilizes the cubic ZrO_2 phase.

Formation of a ZrO_2 layer on the free surface of the MG film implies that the residual amorphous phase becomes depleted in zirconium (or equivalently enriched in copper) which is confirmed by the shift of the broad diffraction maximum. Similar compositional variation effect has been previously reported for $Cu_{30}Zr_{70}$ melt-quenched amorphous ribbons and was related to stabilization of the subsurface region [21]. The stabilization was attributed to a shift of the amorphous phase composition towards the equiatomic one, which exhibits enhanced glass-forming ability. Since $Cu_{67}Zr_{33}$ alloy is close to the Cu-rich limit of the glass-formation range (~70 at% of Cu) [15,16], further increase of the Cu concentration destabilizes the amorphous phase which eventually crystallizes. During conventional annealing experiment crystallization of Cu–Zr MGs proceeds typically by nucleation and growth of one or more intermetallic compounds [10,15,54] which appear in the equilibrium Cu–Zr phase diagram [66]. As mentioned above, we did not observe any traces of Cu-Zr intermetallic compounds within the investigated range of *F* and *N*. To our knowledge, metallic copper has not been previously reported as a crystallization product of Cu–Zr MG. The current experimental results do not allow us to provide an unambiguous explanation of the lack of Cu–Zr intermetallic compounds among the crystallization products, but one can speculate that precipitation of Cu is related to the presence of amorphous phase nano-scale compositional fluctuations detected by TEM both in the as-deposited as well as in laser-irradiated films. Due to the presence of Cu-rich regions, the local nucleation probability of fcc Cu can exceed that of intermetallic Cu–Zr compounds. Similar effect resulting in nanocrystallization of fcc Al and attributed to amorphous phase separation has been observed in Al-rare earth MGs [67]. We note that phase separation has been previously reported for magnetron-sputtered Cu-Zr MG film [68] (same technique as applied for samples investigated in the current study), but not for liquid-quenched ones [69].

The main advantage of the current approach is the possibility to evaluate the crystallization kinetics as well as the microstructure evolution. The changes in relative volume fraction and average grain size of ZrO_2 and Cu shown in Fig. 5 allow comparison of the low- and high-fluence crystallization kinetics. During solidification of an alloy with solid/liquid interfacial kinetics limited by diffusion [70] the maximum of the crystal growth rate is located at higher temperatures than the maximum of crystal nucleation rate. According to data shown in Fig. 5c and d, the growth of grains is detected only for high fluence with no specific trend visible for low fluence. When comparing the grain size evolution with the crystalline phase contribution plotted in Fig. 5a and b, it is clear that at low temperature the increase of the crystalline fraction of both ZrO_2 and Cu is due to increasing number of nano-size grains of approximately constant size while at high temperature the transformation kinetics reflects mainly grain growth. This observation demonstrates that UPLA allows access to fast, high-temperature transformation kinetics which – as predicted for metallic alloys [71] – is dominated by crystal growth.

Apart from general trends, which are similar for ZrO_2 and Cu, the temperature-dependent transformation kinetics (the number of laser pulses required for the transformation to proceed from 5% to 33% as depicted in Fig. 6) is clearly different for the two phases. This difference suggests that while oxidation and crystallization are interrelated processes, their temperature-dependent rates are not identical. From Fig. 6, it can be seen that oxidation accelerates with increasing temperature faster than precipitation of Cu. This observation might be explained by different activation energies for diffusion of atomic species involved in devitrification. It can be argued that while oxidation is controlled by the in-depth diffusion of oxygen through ZrO_2 towards the ZrO_2/glass interface [20], nucleation and growth of Cu are limited by diffusion of Cu in the glassy/supercooled liquid phase. According to the literature, the activation energy for self-diffusion of oxygen in zirconia is about 2 eV [72], while that of Cu in (equilibrium) Cu-Zr liquid is about 0.6 eV [73]. Such a difference in activation energy implies higher temperature sensitivity of oxygen diffusivity as compared to Cu, which is in

agreement with our experimental observations. In the described above scenario, Zr atoms are mostly immobile and the transformation is controlled primarily by an extremely rapid diffusion of oxygen and slower diffusion of Cu. This view is supported by very recent experimental reports showing that the diffusivity of Cu in amorphous/supercooled liquid Cu-Zr alloys greatly exceeds that of Zr [74].

Judging from the SEM data summarized in Fig. 7d, the *N*-dependent fluence thresholds for surface morphology modifications exhibit similar trends to those shown for the onset of the glass-crystal transformation in Fig. 6. However, the thresholds of surface morphology modifications are not fully correlated with the onset of devitrification. A general trend emerging from this comparison is that the devitrification does not start before the ripples form on the surface. The periodic modulation of the material surface after fs-laser irradiation (so called LIPSS - laser-induced periodic surface structures) is a well-known phenomenon occurring both in metals and in dielectrics [52]. The actual origin of LIPSS formation remains not completely understood and the elucidation of the mechanism of surface morphology modifications is beyond the scope of the current work.

5. Summary

In the current work we report on the first application of ultrashort pulsed laser annealing combined with microbeam XRD and TEM characterization for resolving the fast crystallization kinetics of thin-film metallic glasses. The proposed approach is based on ultrafast heating of a thin MG film, which partially devitrifies at elevated temperature, cools down extremely rapidly by heat dissipation into the substrate and remains frozen at room temperature in an intermediate glass-crystal transformation stage. The estimated time scales of the crystallization process resolved by the UPLA range from nanoseconds up to hundreds of microseconds, depending on the fluence of the laser pulses and thus the effective transformation temperature. By probing the subsequent devitrification stages by XRD, TEM and SEM, we follow transformation of thin-film $Cu_{67}Zr_{33}$ MG during UPLA treatment. The results allow us to propose a consistent model of this phase transition. We found that the devitrification process involves the ultra-fast formation of a thin layer of cubic ZrO_2 on the free surface of the film and the precipitation of fcc-Cu in the sub-surface region. Our experimental observations indicate that the transformation kinetics changes from a nucleation-dominated to a growth-dominated mechanism when going from low to high effective annealing temperatures.

As a final remark, we note that besides devitrification, the proposed approach can be successfully applied for resolving of fast, high temperature kinetics of other structural phase transitions in solids stimulated by ultrashort pulsed laser annealing. In particular, the method can be potentially useful for in-situ monitoring of laser-induced surface reactions such as those in catalytically active thin films and coatings.

CRediT authorship contribution statement

J. Antonowicz: Conceptualization, Methodology, Investigation, Writing – original draft, Writing – review & editing, Visualization, Data Curation, Formal analysis, Supervision, Project administration, Funding acquisition. **P. Zalden**: Conceptualization, Methodology, Investigation, Writing – review & editing. **K. Sokolowski-Tinten**: Conceptualization, Methodology, Investigation, Writing – review & editing, Funding acquisition. **K. Georgarakis**: Investigation, Writing - Review & Editing. **R. Minikayev**: Investigation. **A. Pietnoczka**: Investigation. **F. Bertram**: Resources, Investigation, Writing – review & editing. **M. Chaika**: Investigation. **M. Chojnacki**: Investigation. **P. Dłużewski**: Investigation, Writing – review & editing. **K. Fronc**: Investigation, Writing – review & editing. **A.L. Greer**: Conceptualization, Writing – review & editing. **C. Jastrzębski**: Investigation, Writing – review & editing. **D. Klinger**: Investigation. **Ch. Lemke**: Investigation. **O.M. Magnussen**: Resources, Writing – review & editing. **B. Murphy**: Resources, Writing – review & editing. **K. Perumal**: Investigation. **U. Ruett**: Resources, Writing – review & editing. **K.J. Warias**: Resources, Investigation. **R. Sobierajski**: Conceptualization, Methodology, Investigation, Writing – original draft, Writing – review & editing, Visualization, Data Curation, Software, Formal analysis, Supervision, Project administration, Funding acquisition.

Declaration of Competing Interest

The authors declare that they have no known competing financial interests or personal relationships that could have appeared to influence the work reported in this paper.

Acknowledgments

This work was supported by the National Science Centre, Poland, grant agreements No 2017/27/B/ST3/02860 and No 2018/02/X/ST3/00197, the German Federal Ministry of Education and Research (BMBF), Grant No BMBF/05K13FK2/05K16FK1/05K19FK1, and the *Deutsche Forschungsgemeinschaft* (DFG, German Research Foundation) through the Collaborative Research Centre (CRC) 1242 (project number 278162697, project C01 *Structural Dynamics in Impulsively Excited Nanostructures*). We acknowledge DESY (Hamburg, Germany), a member of the Helmholtz Association HGF, for the provision of experimental facilities. Parts of this research were carried out at PETRA III. Beamtime was allocated for proposals: I-20160581 EC, I-20170745 EC and I-20181090 EC. The research leading to this result has been supported by the project CALIPSOplus under the Grant Agreement 730872 from the EU Framework Programme for Research and Innovation HORIZON 2020.

Authors thank K. Jabłońska-Ławniczak and R. Jakieła from Institute of Physics Polish Academy of Sciences for characterization of as-grown samples by means of, respectively XPS and SIMS techniques.

References

[1] A.L. Greer, Metallic glasses, Science vol. 267, (5206) (. 1995) 1947–1953, https://doi.org/10.1126/science.267.5206.1947
[2] A. Inoue, Stabilization of metallic supercooled liquid and bulk amorphous alloys, Acta Mater. 48 (2000) 279–306.
[3] Y.-W. Kim, H.-M. Lin, T.F. Kelly, Amorphous solidification of pure metals in submicron spheres, Acta Met. 37 (1) (1989) 247–255, https://doi.org/10.1016/0001-6160(89)90283-6
[4] L. Zhong, J. Wang, H. Sheng, Z. Zhang, S.X. Mao, Formation of monatomic metallic glasses through ultrafast liquid quenching, Nature 512 (7513) (2014) 177–180, https://doi.org/10.1038/nature13617
[5] D. Turnbull, Metastable structures in metallurgy, Met. Trans. B 12B (1981) 217–230.
[6] J.P. Chu, J. Jang, J.C. Huang, H.S. Chou, Y. Yang, J.C. Ye, Y.C. Wang, J.W. Lee, F.X. Liu, P.K. Liaw, Y.C. Chen, C.M. Lee, C.L. Li, C. Rullyani, Thin film metallic glasses: unique properties and potential applications, Thin Solid Films 520 (16) (2012) 5097–5122, https://doi.org/10.1016/j.tsf.2012.03.092
[7] D.V. Louzguine-Luzgin, T. Hitosugi, N. Chen, S.V. Ketov, A. Shluger, V.Y. Zadorozhnyy, A. Caron, S. Gonzales, C.L. Qin, A. Inoue, Investigation of transparent magnetic material formed by selective oxidation of a metallic glass, Thin Solid Films 531 (2013) 471–475, https://doi.org/10.1016/j.tsf.2013.01.006
[8] D.V. Louzguine-Luzgin, C.L. Chen, L.Y. Lin, Z.C. Wang, S.V. Ketov, M.J. Miyama, A.S. Trifonov, A.V. Lubenchenko, Y. Ikuhara, Bulk metallic glassy surface native oxide: its atomic structure, growth rate and electrical properties, Acta Mater. 97 (2015) 282–290, https://doi.org/10.1016/j.actamat.2015.06.039
[9] A. Inoue, B. Shen, N. Nishiyama, Development and applications of late transition metal bulk metallic glasses, Bulk. Met. Glas. Overv. 18 (2008) 1–25, https://doi.org/10.1007/978-0-387-48921-6_1
[10] K.H. J. Buschow, Thermal stability of amorphous Zr-Cu alloys, vol. 3319, 1981, doi:10.1063/1.329152.
[11] Y. Sato, C. Nakai, M. Wakeda, S. Ogata, Predictive modeling of Time-Temperature-Transformation diagram of metallic glasses based on atomistically-informed

classical nucleation theory, Sci. Rep. 7 (1) (2017) 2–10, https://doi.org/10.1038/s41598-017-06482-8
[12] R. Ray, B.C.C. Giessen, N.J.J. Grant, New non-crystalline phases in splat cooled transition metal alloys, Scr. Met. 2 (6) (1968) 357–359, https://doi.org/10.1016/0036-9748(68)90138-5
[13] H.S. Chen, Y. Waseda, Structure of glassy Zr–Cu and Nb–Ni alloys, Phys. Status Solidi A 51 (1979) 593–599.
[14] J. Antonowicz, A. Pietnoczka, K. Pękała, J. Latuch, G.A. Evangelakis, Local atomic order, electronic structure and electron transport properties of Cu-Zr metallic glasses, J. Appl. Phys. 115 (20) (2014) 203714, https://doi.org/10.1063/1.4879903
[15] Z. Altounian, T. Guo-Hua, J.O. Strom-Olsen, Crystallization characteristics of Cu–Zr metallic glasses from Cu70Zr30to Cu25Zr75, J. Appl. Phys. 53 (7) (1982) 4755–4760, https://doi.org/10.1063/1.331304
[16] N. Mattern, A. Schöps, U. Kühn, J. Acker, O. Khvostikova, J. Eckert, Structural behavior of CuxZr100-x metallic glass (x = 35-70), J. Non Cryst. Solids 354 (10–11) (2008) 1054–1060, https://doi.org/10.1016/j.jnoncrysol.2007.08.035
[17] G.A. Almyras, G.M. Matenoglou, P. Komninou, C. Kosmidis, P. Patsalas, G.A. Evangelakis, On the deposition mechanisms and the formation of glassy Cu-Zr thin films, J. Appl. Phys. 107 (8) (2010), https://doi.org/10.1063/1.3366715
[18] J. Sakurai, S. Hata, A. Shimokohbe, Characteristics of Cu-Zr thin film metallic glasses fabricated using a carousel-type sputtering system, Jpn. J. Appl. Phys. 48 (2) (2009) 025503, https://doi.org/10.1143/JJAP.48.025503
[19] M. Saitou, Cu–Zr thin film electrodeposited from an aqueous solution using rectangular pulse current over a megahertz frequency range, Int. J. Electrochem. Sci. vol. 13, (4) (2018) 3326–3334, https://doi.org/10.20964/2018.04.26
[20] U. Köster, L. Jastrow, Oxidation of Zr-based metallic glasses and nanocrystalline alloys, Mater. Sci. Eng. A 448–451 (2007) 57–62, https://doi.org/10.1016/j.msea.2006.02.316
[21] K.R. Lim, et al., Oxidation induced amorphous stabilization of the subsurface region in Zr- Cu metallic glass, Appl. Phys. Lett. 104 (3) (2014), https://doi.org/10.1063/1.4862025
[22] K.R. Lim, W.T. Kim, D.H. Kim, K. Dh, Characterization of the oxide layer formed on the Cu–Zr based metallic glass during continuous heating, 42 (3) (2012) 174–178, https://doi.org/10.9729/AM.2012.42.3.174
[23] Z. Xu, Y. Xu, A. Zhang, J. Wang, Z. Wang, Oxidation of amorphous alloys, J. Mater. Sci. Technol. 34 (11) (2018) 1977–2005, https://doi.org/10.1016/j.jmst.2018.02.015
[24] K.R. Lim, J.M. Park, S.J. Kim, E.S. Lee, W.T. Kim, A. Gebert, J. Eckert, D.H. Kim, Enhancement of oxidation resistance of the supercooled liquid in Cu–Zr-based metallic glass by forming an amorphous oxide layer with high thermal stability, Corros. Sci. 66 (2013) 1–4, https://doi.org/10.1016/j.corsci.2012.09.018
[25] K.R. Lim, C.E. Kim, Y.S. Yun, W.T. Kim, A. Soon, D.H. Kim, Remarkably stable amorphous metal oxide grown on Zr–Cu–Be metallic glass, Sci. Rep. 5 (2015) 1–8, https://doi.org/10.1038/srep18196
[26] U. Brossmann, R. Würschum, U. Södervall, H.-E. Schaefer, Oxygen diffusion in ultrafine grained monoclinic ZrO2, J. Appl. Phys. 85 (11) (1999) 7646–7654, https://doi.org/10.1063/1.370567
[27] U. Köster, Surface crystallization of metallic glasses, Mater. Sci. Eng. 97 (1988) 233–239, https://doi.org/10.1016/0025-5416(88)90049-3
[28] D.R. Allen, J.C. Foley, J.H. Perepezko, Nanocrystal development during primary crystallization of amorphous alloys, Acta Mater. 46 (1998) 431–440.
[29] J. Antonowicz, Time-resolved X-ray diffraction study of nanocrystallization in Al-based metallic glasses, J. Non Cryst. Solids 351 (30–32) (2005) 2383–2387, https://doi.org/10.1016/j.jnoncrysol.2005.06.037
[30] A.L. Greer, New horizons for glass formation and stability, Nat. Mater. 14 (6) (2015) 542–546, https://doi.org/10.1038/nmat4292
[31] I. Okulov, I. Soldatov, I. Kaban, B. Sarac, F. Spieckermann, J. Eckert, Fabrication of metastable crystalline nanocomposites by flash annealing of Cu47.5Zr47.5Al5 metallic glass using joule heating, Nanomater. (Basel Switz.) 10 (1) (2020), https://doi.org/10.3390/nano10010084
[32] P. Zalden, A. Von Hoegen, P. Landreman, M. Wuttig, A.M. Lindenberg, How supercooled liquid phase-change materials crystallize: snapshots after femtosecond optical excitation, Chem. Mater. 27 (16) (2015) 5641–5646, https://doi.org/10.1021/acs.chemmater.5b02011
[33] C.J. Lin, F. Spaepen, Fe–B glasses formed by picosecond pulsed laser quenching, Appl. Phys. Lett. 41 (8) (1982) 721–723, https://doi.org/10.1063/1.93647
[34] K. Affolter, M. von Allmen, Glass-forming ability in laser quenched transition-metal Alloys, Appl. Phys. A Solids Surf. 33 (2) (1984) 93–96, https://doi.org/10.1007/BF00617614
[35] M. Von Allmen, S.S. Lau, M. Mäenpää, B.Y. Tsaur, Metastable phases in laser-irradiated Pt–Si and Pd–Si thin films, Appl. Phys. Lett. 37 (1) (1980) 84–86, https://doi.org/10.1063/1.91712
[36] A.P. Radliński, A. Calka, B. Luther-Davies, Modification of Pd77Si23 metallic glasses by picosecond laser annealing, Phys. Rev. Lett. 57 (24) (1986) 3081–3084, https://doi.org/10.1103/PhysRevLett.57.3081
[37] A. Calka, A.P. Radliński, Laser pulse crystallization of Pd–Si metallic glasses, J. Mater. Sci. 21 (1986) 1786–1792, https://doi.org/10.1007/BF01114740
[38] M. Von Allmen, S.S. Lau, M. Mäenpää, B.Y. Tsaur, Phase transformations in laser-irradiated Au–Si thin films, Appl. Phys. Lett. 36 (3) (1980) 205–207, https://doi.org/10.1063/1.91426
[39] Y. Li, Q. Guo, J.A. Kalb, C.V. Thompson, Matching glass-forming ability with the density of the amorphous phase, Science 322 (5909) (2008) 1816–1819, https://doi.org/10.1126/science.1163062
[40] O.H. Seeck, C. Deiter, K. Pflaum, F. Bertam, A. Beerlink, H. Franz, J. Horbach, H. Schulte-Schrepping, B.M. Murphy, M. Greve, O. Magnussen, The high-resolution diffraction beamline P08 at PETRA III, J. Synchrotron Radiat. 19 (1) (2012) 30–38, https://doi.org/10.1107/S0909049511047236
[41] R. Sobierajski, M. Jurek, J. Chalupský, J. Krzywinski, T. Burian, S.D. Farahani, V. Hájková, M. Harmand, L. Juha, D. Klinger, R.A. Loch, C. Ozkan, J.B. Pełka, K. Sokolowski-Tinten, H. Sinn, S. Toleikis, K. Tiedtke, T. Tschentscher, H. Wabnitz, J. Gaudin, Experimental set-up and procedures for the investigation of XUV free electron laser interactions with solids, J. Inst. 8 (2) (2013) P02010, https://doi.org/10.1088/1748-0221/8/02/P02010
[42] J.M. Liu, Simple technique for measurements of pulsed Gaussian-beam spot sizes, Opt. Lett. 7 (5) (1982) 196–198, https://doi.org/10.1364/OL.7.000196
[43] S. Marinier, L.J. Lewis, Femtosecond laser ablation of CuxZr1-x bulk metallic glasses: a molecular dynamics study, Phys. Rev. B Condens. Matter Mater. Phys. 92 (18) (2015) 1–9, https://doi.org/10.1103/PhysRevB.92.184108
[44] O. Arnon, P. Baumeister, Electric field distribution and the reduction of laser damage in multilayers, Appl. Opt. 19 (11) (1980) 1853–1855, https://doi.org/10.1364/AO.19.001853
[45] T. Jeong, J.-G. Zhu, S. Chung, M.R. Gibbons, Thermal boundary resistance for gold and CoFe alloy on silicon nitride films, J. Appl. Phys. 111 (8) (2012) 083510, https://doi.org/10.1063/1.3703571
[46] T. Wang, T.E. Cullinan, R.E. Napolitano, A new method for measuring the thermodynamic properties of undercooled liquid and amorphous Cu–Zr alloys, Acta Mater. 62 (1) (2014) 188–196, https://doi.org/10.1016/j.actamat.2013.09.047
[47] O. Kubaschewski, C.B. Alcock, P.J. Spencer, Materials Thermochemistry. Revised 1993 Pergamon Press Ltd, Head. Hill Hall, Oxford OX 3 0 BW, UK, 1993, p. 363.
[48] G. Ashiotis, A. Deschildre, Z. Nawaz, J.P. Wright, D. Karkoulis, F.E. Picca, J. Kieffer, The fast azimuthal integration Python library: PyFAI, J. Appl. Crystallogr. 48 (2015) 510–519, https://doi.org/10.1107/S1600576715004306
[49] Y. Waseda, E. Matsubara, K. Shinoda, X-Ray Diffraction Crystallography (Berlin Heidelberg), Springer, Berlin, Heidelberg, 2011.
[50] J.E. Jaffe, R.A. Bachorz, M. Gutowski, Low-temperature polymorphs of ZrO2 and HfO2: a density-functional theory study, Phys. Rev. B 72 (14) (2005) 144107, https://doi.org/10.1103/PhysRevB.72.144107
[51] M.E. Straumanis, L.S. Yu, Lattice parameters, densities, expansion coefficients and perfection of structure of Cu and of Cu–In α phase, Acta Crystallogr. Sect. A 25 (6) (1969) 676–682, https://doi.org/10.1107/S0567739469001549
[52] J. Bonse, J. Krüger, S. Höhm, A. Rosenfeld, Femtosecond laser-induced periodic surface structures, J. Laser Appl. 24 (4) (2012) 042006, https://doi.org/10.2351/1.4712658
[53] J. Chalupský, T. Burian, V. Hájková, L. Juha, T. Polcar, J. Gaudin, M. Nagasono, R. Sobierajski, M. Yabashi, J. Krzywinski, Fluence scan: an unexplored property of a laser beam, Opt. Express 21 (22) (2013) 26363–26375, https://doi.org/10.1364/oe.21.026363
[54] I. Kalay, Devitrification kinetics and phase selection mechanisms in Cu-Zr metallic glasses, Jan. 2010, doi:10.2172/1037980.
[55] R. Nielsen, "Zirconium and Zirconium Compounds," Ullmann's Encyclopedia of Industrial Chemistry. Jun. 15, 2000, doi:10.1002/14356007.a28_543.
[56] D. Huang, L. Huang, B. Wang, V. Ji, T. Zhang, The relationship between t-ZrO 2 stability and the crystallization of a Zr-based bulk metallic glass during oxidation, Intermetallics 31 (2012) 21–25, https://doi.org/10.1016/j.intermet.2012.05.009
[57] W. Kai, W.S. Chen, Y.H. Wu, P.C. Lin, C.P. Chuang, P.K. Liaw, Air-oxidation of a Cu50Zr50 binary amorphous ribbon at 350–425 °C, J. Alloys Compd. 536 (2012) S103–S108, https://doi.org/10.1016/J.JALLCOM.2011.12.175
[58] H.H. Hsieh, W. Kai, W.L. Jang, R.T. Huang, P.Y. Lee, W.H. Wang, The oxidation behavior of Cu–Zr–Ti-base bulk metallic glasses in air at 350–500 °C, Oxid. Met. 67 (3–4) (2007) 179–192, https://doi.org/10.1007/s11085-007-9049-y
[59] F. Zhang, P.J. Chupas, S. Lui, J.C. Hanson, W.A. Caliebe, P.L. Lee, S.W. Chan, In situ study of the crystallization from amorphous to cubic zirconium oxide: rietveld and reverse Monte Carlo analyses, Chem. Mater. 19 (13) (2007) 3118–3126, https://doi.org/10.1021/cm061739w
[60] R.C. Garvie, M.F. Goss, Intrinsic size dependence of the phase transformation temperature in zirconia microcrystals, J. Mater. Sci. 21 (4) (1986) 1253–1257, https://doi.org/10.1007/BF00553259
[61] P. Pramanik, S. Singh, D.C. Joshi, A. Mallick, K. Pisane, A.H. Romero, S. Thota, M.S. Seehra, Cubic phase stability, optical and magnetic properties of Cu-stabilized zirconia nanocrystals, J. Phys. D Appl. Phys. 51 (22) (2018) 225304, https://doi.org/10.1088/1361-6463/aac004
[62] P.M. Smith, R. Reitanot, M.J. Aziz, Solute trapping in metals, MRS Proc. 279 (1992) 749, https://doi.org/10.1557/PROC-279-749
[63] P. Galenko, Solute trapping and diffusionless solidification in a binary system, Phys. Rev. E Stat. Nonlin Soft Matter Phys. 76 (3) (2007) 031606, https://doi.org/10.1103/PhysRevE.76.031606
[64] M.J. Aziz, Interface attachment kinetics in alloy solidification, Metall. Mater. Trans. A 27 (3) (1996) 671–686, https://doi.org/10.1007/BF02648954
[65] A. Dhawan, V. Zaporojtchenko, F. Faupel, S.K. Sharma, Study of air oxidation of amorphous Zr65Cu17.5Ni 10Al7.5 by X-ray photoelectron spectroscopy (XPS), J. Mater. Sci. 42 (21) (2007) 9037–9044, https://doi.org/10.1007/s10853-007-1819-z
[66] H. Okamoto, Cu–Zr (Copper-Zirconium), J. Phase Eqilib. Diffusion 29 (2) (2008) 204, https://doi.org/10.1007/s11669-008-9267-2
[67] J. Antonowicz, A.R. Yavari, W.J. Botta, P. Panine, Phase separation and nanocrystallization in Al92Sm8 metallic glass, Philos. Mag. 86 (27) (2006) 4235–4242, https://doi.org/10.1080/14786430500375175
[68] T.W. Barbee, R.G. Walmsley, A.F. Marshall, D.L. Keith, D.A. Stevenson, Phase separation in vapor quench synthesized noncrystalline copper zirconium alloys, Appl. Phys. Lett. 38 (3) (1981) 132–135, https://doi.org/10.1063/1.92275

[69] N. Mattern, U. Kühn, A. Concustell, A. Schöps, M.D. Baro, J. Eckert, Phase separation and crystallization in Cu–Zr metallic glasses, Mater. Trans. 48 (7) (2007) 1639–1643, https://doi.org/10.2320/matertrans.MJ200708
[70] K.F. Kelton, A.L. Greer, Nucleation in Condensed Matter: Applications in Materials and Biology, Pergamon Materials Series, 2010.
[71] A.L. Greer, Grain refinement in rapidly solidified alloys, Mater. Sci. Eng. A 133 (1991) 16–21, https://doi.org/10.1016/0921-5093(91)90006-9
[72] J. Yang, M. Youssef, B. Yildiz, Oxygen self-diffusion mechanisms in monoclinic ZrO2 revealed and quantified by density functional theory, random walk analysis, and kinetic Monte Carlo calculations, Phys. Rev. B 97 (2) (2018) 1–7, https://doi.org/10.1103/PhysRevB.97.024114
[73] F. Yang, D. Holland-Moritz, J. Gegner, P. Heintzmann, F. Kargl, C.C. Yuan, G.G. Simeoni, A. Meyer, Atomic dynamics in binary Zr–Cu liquids, Epl 107 (4) (2014) 46001, https://doi.org/10.1209/0295-5075/107/46001
[74] S.V. Ketov, Y.P. Ivanov, B. Putz, Z. Zhang, J. Eckert, A.L. Greer, Atomic diffusivities in amorphous and liquid Cu–Zr: Kirkendall effects and dependence on packing density, Acta Mater. 214 (2021) 116993, https://doi.org/10.1016/j.actamat.2021.116993

2021-08-03

Devitrification of thin film Cu-Zr metallic glass via ultrashort pulsed laser annealing

Antonowicz, J.

Elsevier

Antonowicz J, Zalden P, Sokolowski-Tinten K, et al., (2021) Devitrification of thin film Cu-Zr metallic glass via ultrashort pulsed laser annealing. Journal of Alloys and Compounds, Volume 887, December 2021, Article number 161437

https://doi.org/10.1016/j.jallcom.2021.161437